International Journal of Oral Science www.nature.com/ijos

ARTICLE OPEN

ANKRD1 sustains a neurogenic BMSC niche and counters cognitive aging

Zifei Wang[1], Xiaoyun Liu[1], Wenyu Zhen[1], Fei Xu[1], Rui Wang[1], Wenhu Fan[2], Wenhao Zhang[1], Yulong Zhang[1], Wansu Sun[1], Mingyue Wu[1], Jiacai He[1]✉, Hao Gu[2]✉ and Hengguo Zhang[1]✉

Craniomaxillofacial bone marrow mesenchymal stromal cells (BMSCs) retaining neural crest–derived neurogenic niche is driven by lineage memory and niche homeostasis. Elucidating how the neurogenic potential is maintained is critical for neurological health. Here, we explored a neural crest-like progenitor niche in BMSCs with high neurogenic and proliferative capacity by single-cell transcriptomics. In which, ANKRD1 is a pivotal regulator sustaining the neurogenic reservoir. Importantly, ANKRD1 expression in this niche declines with aging and lineage commitment, coinciding with its redistribution from a diffuse nucleoplasmic pattern to perinuclear enrichment along the nuclear lamina and loss of neural potential. Mechanistically, ANKRD1 preserves neurogenic capacity by directly binding super-enhancers of neural marker genes (SOX2, NESTIN) and maintaining open chromatin architecture. Critically, neuron-targeted ANKRD1 delivery rescues spatial memory deficits in aged mice. These findings establish ANKRD1 as a therapeutically tractable regulator that sustains neurogenic chromatin reservoirs to support neurocognitive resilience, opening avenues to counter cognitive aging.

International Journal of Oral Science (2026)18:23 ; https://doi.org/10.1038/s41368-026-00428-5

INTRODUCTION

Craniofacial bone marrow mesenchymal stromal cells (BMSCs) derived from neural crest stem cells (NCSCs), which represent a transient embryonic progenitor population endowed with diverse lineages, including peripheral neurons and glia.[1–3] Emerging evidence suggests adult BMSCs retain traces of their NCSCs heritage, exhibiting latent neurogenic plasticity that could be harnessed for neural repair.[4,5] Despite progress in characterizing BMSCs multipotency,[6] the transcriptional circuits preserving their neural competence during aging and the mechanisms by which they deteriorate remain unresolved. Understanding these dynamics is critical for leveraging BMSCs-based therapies against neurodegenerative disorders.

Neural crest cells originate from neuroepithelial cells, in which SOX2 and NESTIN serve as key markers for maintaining neural progenitor identity during embryonic development.[7–9] SOX2, a pivotal transcription factor and the earliest marker of the neural plate, is essential for early embryogenesis and embryonic stem cells (ESCs) pluripotency.[10,11] Importantly, SOX2 transcription in mouse ESCs is primarily governed by a 7.3-kb cluster of transcription factor-binding regions located downstream of the gene (>100 kb). Notably, both the SOX2 locus and its regulatory elements reside at the boundary of an ESCs-specific topologically associated domain (TAD), which disassembles upon differentiation.[12–14] Further evidence demonstrates that SOX2 enhancer clusters form spatial hubs within TADs, orchestrating gene expression via chromatin looping.[13,15,16] As another critical neuroepithelial marker, NESTIN is the intermediate filament protein widely utilized to identify neural precursor cells.[17,18] Transgenic mouse studies confirm that the tissue-specific enhancer embedded in the second intron of the NESTIN gene is capable of driving endogenous NESTIN expression.[18,19] While enhancer remodeling has been implicated in neural specification in pluripotent stem cells, whether similar mechanisms sustain neurogenic memory in adult stem cells, such as BMSCs remains unexplored.[20,21] As a result, identifying factors that stabilize these critical regulatory architectures in adult progenitors could illuminate new avenues to counteract neurocognitive decline.

Ankyrin repeat domain 1 (ANKRD1), also known as cardiac ankyrin repeat protein (CARP), is a conserved member of the ankyrin repeat protein family.[22] In humans, the ANKRD1 gene is located on chromosome 10 and exhibits high evolutionary conservation among mammals.[23] While ANKRD1 has been primarily characterized as a transcriptional coactivator in cardiac pathophysiology,[24–26] skin wound healing,[27,28] and oncogenesis,[29–31] emerging evidence implicates its functional role in neural regeneration. For instance, ANKRD1 modulates microtubule dynamics in neurons, influencing axonal architecture and transport.[32] Additionally, it contributes to the stabilization of tyrosine hydroxylase (TH) and catecholamine biosynthesis for the transmission of neural signals.[33] Despite these findings, the potential role of ANKRD1 in neurogenic remodeling remains poorly understood.

In this study, through scRNA-seq of human BMSCs, we discovered a discrete subpopulation exhibiting molecular signatures of neurogenic potential. Gene enrichment analysis identified ANKRD1 as a top-scoring candidate, and subsequent validation studies confirmed its role as a key regulator of this neurogenic phenotype. We propose that ANKRD1 may sustain neurogenic competence in undifferentiated BMSCs, a capacity that is progressively eroded by aging or differentiation-associated

[1]College & Hospital of Stomatology, Anhui Medical University, Anhui Provincial Key Laboratory of Oral Diseases Research, Anhui Medical University, Hefei, China and [2]Department of Immunology, the School of Basic Medical Sciences, Anhui Medical University, Hefei, China
Correspondence: Jiacai He (hejiacai@163.com) or Hao Gu (guhao@ahmu.edu.cn) or Hengguo Zhang (zhanghengguo@ahmu.edu.cn)

Received: 14 August 2025 Revised: 16 January 2026 Accepted: 19 January 2026
Published online: 01 March 2026

transcriptional reprogramming. Mechanistically, protein-DNA interaction profiling revealed that ANKRD1 directly engages with enhancer elements of SOX2 and NESTIN, thereby preserving their expression and reinforcing neural-lineage characteristics. Strikingly, in vivo studies demonstrated that ANKRD1 targeting ameliorates neurocognitive aging in animal models, implicating its therapeutic potential. Our findings illuminate ANKRD1 as a novel guardian of neurogenic plasticity in BMSCs. Deciphering its regulatory axis may unlock new strategies for neural regeneration, offering a theory basis to harness endogenous adult stem cell potential for neurological repair.

RESULTS

ANKRD1 is a vital marker gene in neural progenitor BMSCs

To profile the neurogenic potential related molecular signatures of neural crest-derived BMSCs, we analyzed single-cell RNA sequencing data of human BMSCs. Using UMAP dimensionality reduction and clustering, we mapped six distinct cell clusters (0–5) based on transcriptomic profiles and classified clusters according to cell cycle phases (G1, S, G2M) (Fig. 1a). We observed that clusters 0–5 predominantly occupied the G1, S, and G2M phases, indicating heightened proliferative activity (Fig. 1a). Then, partition-based graph abstraction (PAGA) analysis demonstrated the connectivity between these six clusters, with cluster sizes and transition probabilities reflected by node size and string thickness, respectively (Fig. 1b). Further pseudotime trajectory analysis identified a developmental progression from a progenitor state (Pre) to differentiated states (Fate1 and Fate2), with cluster 4 (purple) as a progenitor population occupied the earliest position on the trajectory and exhibited the lowest pseudotime value (Fig. 1c, d). These data suggest that cluster 4 may represent as a progenitor state in BMSCs.

To further characterize the progenitor state, we conducted differential gene expression heatmapping and top-ranked pathway enrichment analysis. The finding revealed progressive downregulation of neural crest progenitor-associated genes during progenitor state toward differentiated states (Fig. 1e). Meanwhile, we identified a significant enrichment of neurodegenerative pathways including Parkinson's, Alzheimer's, and Huntington's diseases–implying a significantly decline of neural function in the process of differentiation (Fig. 1f). Subsequently enrichment analysis of marker genes in cluster 4 illustrated the core transcriptomic network driving its biological identity. Among the top 25 elevated markers, key cell cycle regulators (TOP2A, PCNA, MKI67, CENPF) showed pronounced upregulation, indicating robust proliferative capacity (Fig. 1g). Moreover, violin plot analysis captured concurrent enrichment of neural sensors (PIEZO1, PIEZO2, ORAI1, FUS, SCN9A) and pro-proliferative transcription factors (KLF4, KLF2, MAPK1, SON, HMGB2) (Fig. S1a). These findings collectively show cluster 4 as a self-renewing neuroprogenitor niche with intrinsically coupled proliferative and neural developmental capacities.

Given the established association between progenitor-like BMSCs and neural development, we sought to identify specific markers governing their neurogenic potential. To this end, we incubated BMSCs in neural stem cells (NSCs) medium (3 days). The results revealed a robust upregulation of peripheral nervous system markers (NGFR, SOX10, S100B) following induction (Figs. 1h and S1b). Furthermore, qPCR quantification of top-enriched genes in cluster 4 (excluding proliferation-associated genes) demonstrated upregulated expression of multiple top genes, suggesting their critical role in maintaining BMSCs' neurogenic properties (Fig. 1i). Among all the genes, ANKRD1 exhibited significantly higher expression under induction (Figs. 1i and S1c), demonstrating its potential involvement in neural health and neurogenic function. These findings implicate the potential role of ANKRD1 in sustaining neural progenitor characteristics of BMSCs.

Downregulation and blocked nuclear localization of ANKRD1 in aging BMSCs

Craniofacial morphogenesis originates from neural crest cells (NCCs), the neurogenic properties diminish progressively and concomitant with cellular senescence during organismal aging.[34–36] To investigate the role of ANKRD1 in this process, we first examined its involvement in the aging of BMSCs. As expected, ANKRD1 expression was significantly downregulated in replicative senescent BMSCs, revealing consistent suppression at both transcriptional and translational levels during BMSC aging (Fig. 2a, b). Critically, parallel evaluation of ANKRD1 expression in BMSCs isolated from human donors with different ages echoed these findings, which further validating an age-associated attenuation of this neurogenic regulator (Fig. 2c). To further investigate whether ANKRD1 regulates the senescence phenotype of BMSCs, we overexpressed ANKRD1 in aged BMSCs and knocked down its expression using shRNA in young BMSCs. We then evaluated both mRNA and protein levels of key senescence-associated secretory phenotype (SASP) components, along with classical cellular senescence markers (p53, p21, and p16). The results shown that knockdown of ANKRD1 in young BMSCs resulted in a marked upregulation of all examined senescence and SASP markers (Fig. 2d, e), while overexpression of ANKRD1 in aged BMSCs led to a significant downregulation of these markers (Fig. S2a, b). These findings indicate that ANKRD1 actively suppresses senescence-associated phenotypes and plays a crucial role in preserving the youthful, proliferative state of BMSCs.

Moreover, immunofluorescence analysis further revealed that cellular senescence triggers both quantitative decrease and spatial reorganization of ANKRD1 (Fig. 2f). This underwent nuclear relocalization from a diffuse nucleoplasmic pattern to perinuclear enrichment along the nuclear lamina (Fig. 2f). These dynamic changes suggest that ANKRD1 may serve as a key transcriptional regulator in BMSCs, and that its regulatory activity is substantially impaired during cellular senescence, potentially contributing to the progressive loss of stemness and neurogenic potential.

ANKRD1 maintains the multipotent state of BMSCs

Previous studies found that the neurogenic characteristics of BMSCs disappeared quickly after terminal osteogenic differentiation.[37] To profiled dynamics ANKRD1 expression during BMSCs lineage differentiation, BMSCs were subjected to osteogenic and adipogenic induction media. Successful osteogenesis was confirmed by Alizarin Red S staining of mineralized nodules, while adipogenesis was verified through Oil Red O visualization of lipid droplets (Fig. 3a, d). We found that terminally differentiated BMSCs exhibited a pronounced reduction of ANKRD1 expression compared to undifferentiated controls (Fig. 3b, c, e, f). To further explore the relationship between ANKRD1 expression and the differentiation status of BMSCs, we performed ANKRD1 knockdown and overexpression experiments. The results showed that knockdown of ANKRD1 significantly upregulated both osteogenic markers (ALPL and Osterix) and adipogenic markers (CEBPA and PPARγ) (Fig. S2c–f). In contrast, overexpression of ANKRD1 led to marked downregulation of these lineage-specific markers (Fig. 3g–j). These findings indicate that ANKRD1 plays a critical role in suppressing premature lineage commitment, thereby helping to preserve the multipotent, undifferentiated state of BMSCs.

ANKRD1 occupies super-enhancers to sustain multipotency in BMSCs

To further elucidate the mechanisms underlying ANKRD1-mediated maintenance of multipotency, we comprehensively profiled its genome-wide occupancy using Cleavage Under Targets and Tagmentation (CUT&TAG) in undifferentiated and osteogenic-differentiated BMSCs. Peak distribution analysis revealed prominent enrichment of ANKRD1 binding sites around transcription start sites (TSSs), indicating a primary role in

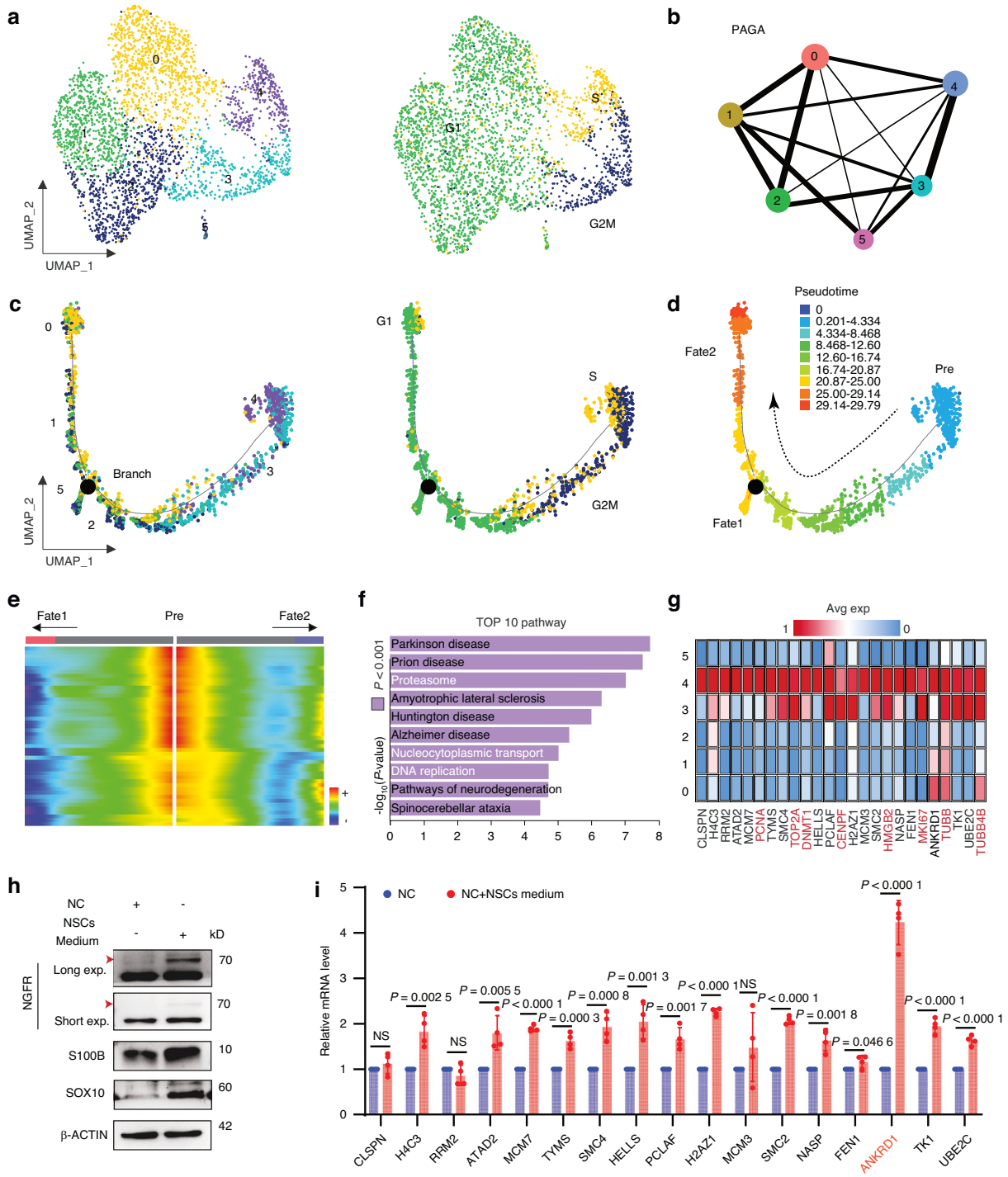

Fig. 1 ANKRD1 is a vital marker gene in neural progenitor BMSCs. **a** Uniform Manifold Approximation and Projection (UMAP) plot derived from single-cell RNA sequencing data from Gene Expression Omnibus (GEO) repositories (GSE113253) reveals transcriptional heterogeneity within BMSCs. Color-coded and numerically labeled clusters represent distinct subpopulations, demonstrating the diversity of transcriptional states present in the BMSCs (left panel). UMAP projection of single-cell RNA sequencing data delineates BMSCs by cell cycle phase (G1, S, G2/M), characterized by a dominant G1-phase population alongside smaller but distinct S-phase and G2/M-phase subsets (right panel). **b** Partition-based graph abstraction (PAGA) was employed to analyze and visualize differentiation trajectories. **c**, **d** Pseudotime trajectory analysis of single-cell transcriptomes visualizing developmental progression from progenitor to differentiated states. Cluster 4 (purple), identified as the progenitor population (Pre) with the lowest pseudotime values, occupies the trajectory origin before branching into two distinct differentiated states (Fate1 and Fate2). **e** Differential gene expression heatmapping reveals progressive downregulation of neural crest progenitor-associated genes during Pre toward Fate 1 and Fate 2 trajectories. **f** Kyoto Encyclopedia of Genes and Genomes (KEGG) enrichment analysis during Pre toward Fate 1 and Fate 2 trajectories. The bar plots display the top 10 enriched terms. **g** Top 25 elevated marker genes in cluster 4. **h** Western blotting against neural markers in BMSCs cultured in NSCs medium (DMEM/F12 + 1 × B27 + 20 ng/mL bFGF + 20 ng/mL EGF + 1%–2% penicillin-streptomycin) versus untreated controls. **i** QRT-PCR analysis of cluster 4-enriched genes (non-proliferative) in NSCs-treated versus untreated BMSCs

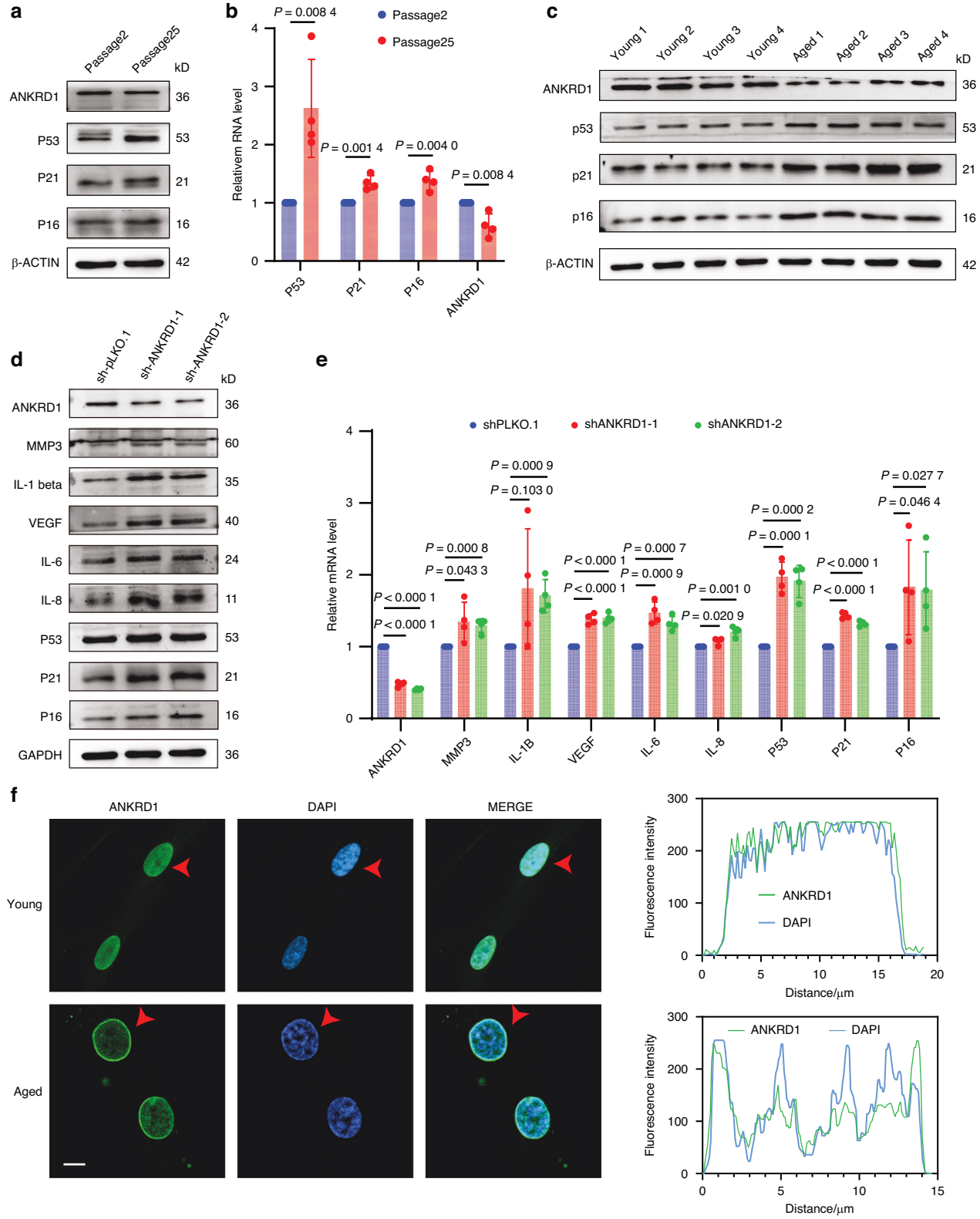

Fig. 2 Downregulation and blocked nuclear localization of ANKRD1 in aging BMSCs. **a** Western blot analysis of ANKRD1 and senescence-associated markers (p53, p21, and p16) in early-passage (passage 2) and late-passage (passage 25) BMSCs. **b** qRT-PCR quantification of mRNA levels of ANKRD1 and senescence-associated markers in passage 2 and passage 25 BMSCs. **c** Western blot analysis of ANKRD1 and senescence-associated markers in BMSCs derived from young (26–33 years) and aged (66–78 years) donors. **d** Western blot analysis of senescence-associated markers in young BMSCs transduced with control vector (shPLKO.1) or ANKRD1-specific shRNAs (shANKRD1-1 and shANKRD1-2). **e** qRT-PCR analysis of senescence-associated markers in young BMSCs transduced with control vector (shPLKO.1) or ANKRD1-specific shRNAs (shANKRD1-1 and shANKRD1-2). **f** Representative high-magnification immunofluorescence images of ANKRD1 staining in young (upper panels) and aged (lower panels) BMSCs. Nuclei were counterstained with DAPI (blue). Scale bar, 10 μm

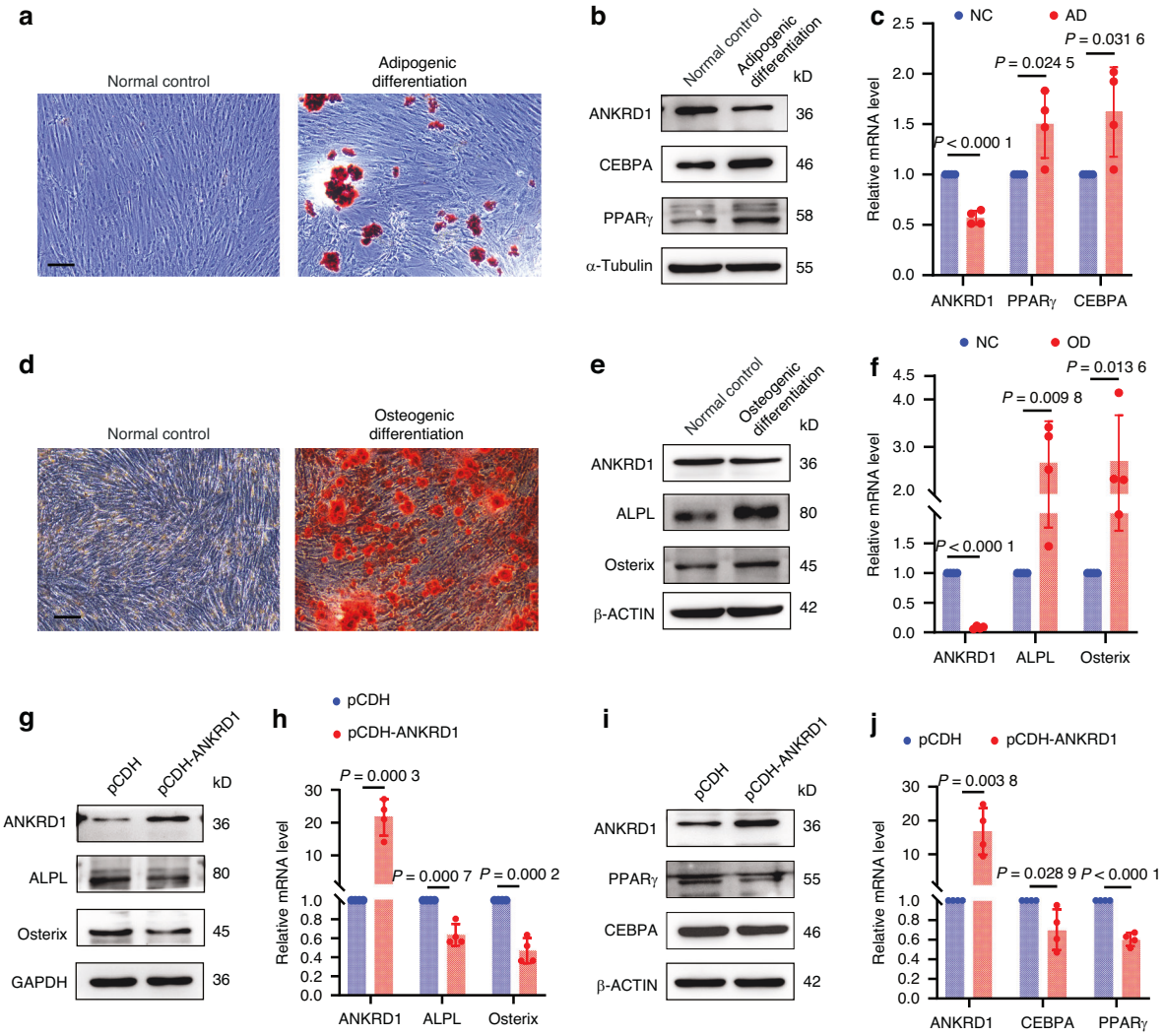

Fig. 3 ANKRD1 maintains the multipotent state of BMSCs. **a** Oil Red O staining of lipid droplets in BMSCs after 21 days of adipogenic induction in vitro. Scale bar, 40 μm. **b**, **c** Western blot and qRT-PCR analyses of ANKRD1 and adipogenic markers (CEBPα and PPARγ) in control and adipogenic-induced BMSCs (21 days). **d** Alizarin Red S staining of mineralized nodules in BMSCs after 21 days of osteogenic induction in vitro. Scale bar, 40 μm. **e**, **f** Western blot and qRT-PCR analyses of ANKRD1 and osteogenic markers (ALPL and Osterix) in control and osteogenic-induced BMSCs (21 days). **g**, **h** Western blot and qRT-PCR analyses of ANKRD1 and osteogenic markers (ALPL and Osterix) in BMSCs transduced with empty vector (pCDH) or ANKRD1 overexpression vector (pCDH-ANKRD1). **i**, **j** Western blot and qRT-PCR analyses of ANKRD1 and adipogenic markers (CEBPA and PPARγ) in BMSCs transduced with empty vector (pCDH) or ANKRD1 overexpression vector (pCDH-ANKRD1)

transcriptional initiation (Fig. S3a, b). Principal component analysis (PCA) clearly separated undifferentiated from osteogenic-differentiated BMSCs, confirming distinct chromatin landscapes (Fig. 4a). Genomic distribution analysis shown that the proportions of ANKRD1 peaks in promoters, introns, exons, and proximal intergenic regions remained largely unchanged during differentiation, whereas the proportion in distal intergenic regions decreased significantly (Figs. 4b and S3c). These observations led us to hypothesize that differentiation may impair ANKRD1-dependent long-range regulatory interactions with distal genes.

We next identified active super-enhancers (SEs) using the ROSE algorithm, detecting 1 401 SEs in undifferentiated BMSCs compared to only 458 in differentiated cells (Fig. 4c). Gene Ontology (GO) biological process enrichment analysis of genes associated with the top 100 ANKRD1-bound SEs revealed striking enrichment for neurogenic pathways—including axon guidance, neuronal migration, and axonogenesis—in undifferentiated BMSCs. In contrast, these neural-related signals were markedly diminished in the differentiated group (Fig. 4c). Notably, strong ANKRD1 occupancy was observed at SEs associated with key neural determinants SOX2 and NESTIN exclusively in undifferentiated BMSCs (Fig. 4c).

To directly evaluate ANKRD1's functional interaction with SOX2- and NESTIN-associated enhancer regions, we constructed luciferase reporter plasmids harboring these elements and co-transfected them with a Renilla normalization control. Overexpression of ANKRD1 significantly activated both SOX2 and NESTIN enhancer-driven luciferase activity, whereas ANKRD1 knockdown markedly suppressed it; co-overexpression effectively rescued the repression (Fig. S4a, b). Furthermore, under osteogenic and adipogenic induction conditions—where enhancer activity normally declined—ANKRD1 overexpression substantially restored reporter signals (Fig. S4a, b). Together, these data demonstrate that ANKRD1 preserves BMSC progenitor identity by directly engaging neurogenic chromatin domains and maintaining the activity of key neural super-enhancers, particularly those governing SOX2 and NESTIN.

Given that ANKRD1 robustly activates NSC marker genes in undifferentiated BMSCs, we next asked whether it also enhances overall stemness. We found overexpression of ANKRD1 significantly

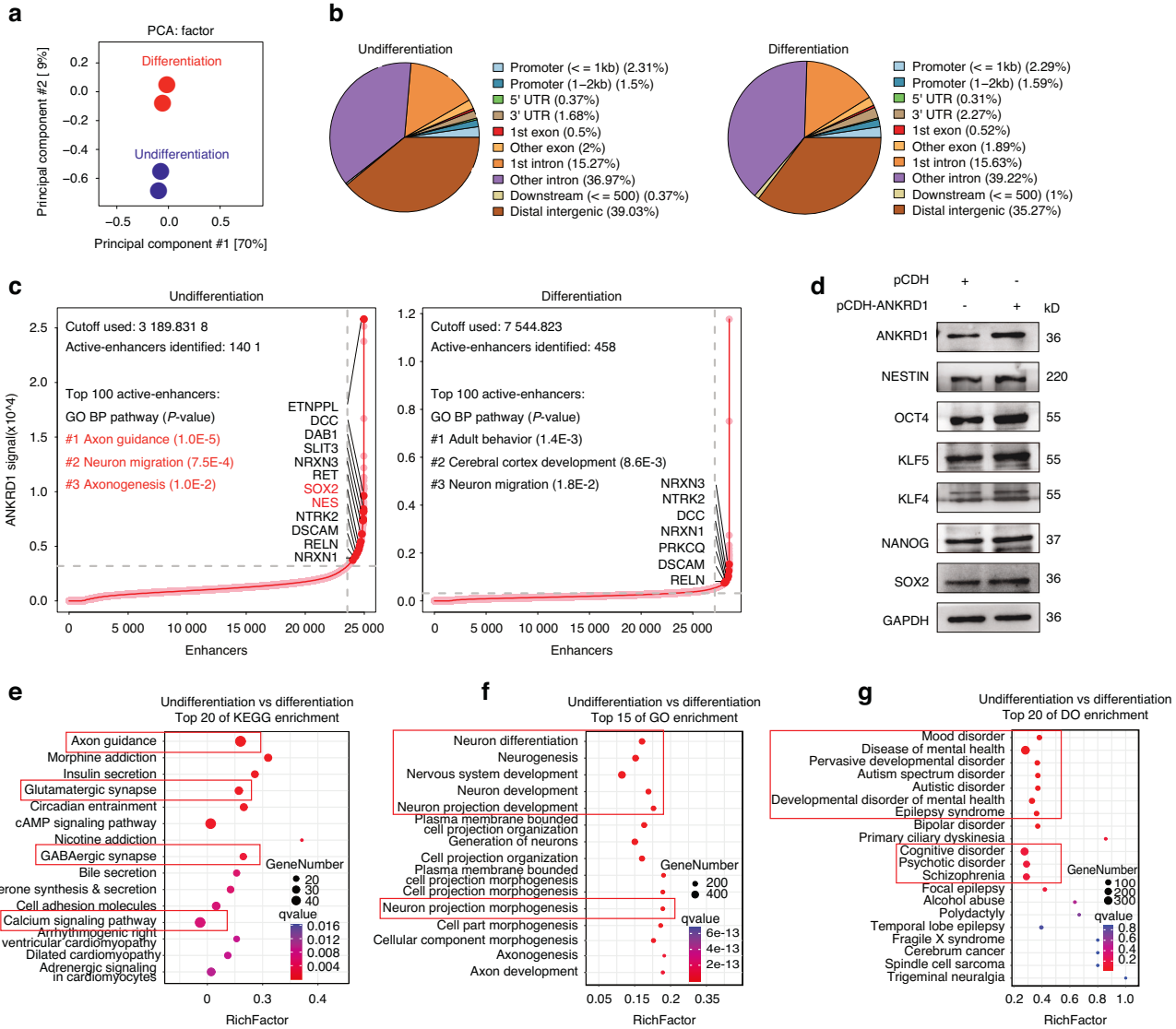

Fig. 4 ANKRD1 occupies super-enhancers to sustain multipotency in BMSCs. **a** Principal Component Analysis (PCA) plot showing clear separation between undifferentiated (blue spheres) and differentiated (Induced osteogenic differentiation) (red spheres) BMSCs ($n = 2$/group). **b** Pie charts depicting the positional annotation of ANKRD1 CUT&TAG peaks, classified by genomic features in priority order: promoters, 5′ UTRs, 3′UTRs, exons, introns, downstream region, and distal intergenic regions. **c** Hockey stick plots of the rank order of ANKRD1 signals for all enhancers in undifferentiated and differentiated BMSCs. Inserted panels of selected GO functional categories of active SE-associated genes. The red arrow indicates the neuro-related SEs. **d** Western blotting analysis of ANKRD1 and stem-related markers (NESTIN, OCT4, KLF5, KLF4, NANOG, SOX2) in BMSCs following transduction with pCDH and pCDH-ANKRD1. (**e**–**g**) KEGG, GO and disease ontology (DO) enrichment analysis on differential peaks in ANKRD1 CUT&TAG data between undifferentiated and differentiated groups

upregulated multiple stemness-associated genes (OCT4, KLF4, KLF5, NANOG, and SOX2) (Figs. 4d and S4c). These findings were further corroborated by RNA-seq transcriptome profiling following ANKRD1 overexpression, which showed consistent changes in stemness-related gene expression (Fig. S4d), supporting a role for ANKRD1 in reinforcing the multipotent state. Furthermore, we also performed Kyoto Encyclopedia of Genes and Genomes (KEGG), Gene Ontology (GO), and Disease Ontology (DO) enrichment analyses on genes associated with differential ANKRD1 binding peaks between undifferentiated and differentiated BMSCs. KEGG pathway analysis revealed significant enrichment in neurogenic signaling pathways in the undifferentiated group, including axon guidance, glutamatergic synapse, GABAergic synapse, and calcium signaling (Fig. 4e). GO biological process analysis highlighted prominent terms related to neuron differentiation, neurogenesis, and axon projection (Fig. 4f). DO analysis further uncovered strong associations with neuropsychiatric and cognitive disorders in the undifferentiated group (Fig. 4g). Taken together, these results position ANKRD1 as a central epigenetic regulator that sustains the neurogenic potential of BMSCs in their progenitor state by directly modulating core neurodevelopmental programs.

ANKRD1 sustains divergent chromatin dynamics at SOX2 and NESTIN loci in BMSCs

SOX2 and NESTIN are hallmark markers of neuroepithelial progenitors, exhibiting dynamic expression patterns during organismal development.[38,39] To further interrogate their chromatin dynamics during BMSC differentiation and aging, we integrated Hi-C and CUT&TAG multi-omics analyses across undifferentiated, differentiated, and aged states. Our results revealed distinct behaviors at these loci. SOX2 stably resides at topological associating domain (TAD) boundaries, preserving

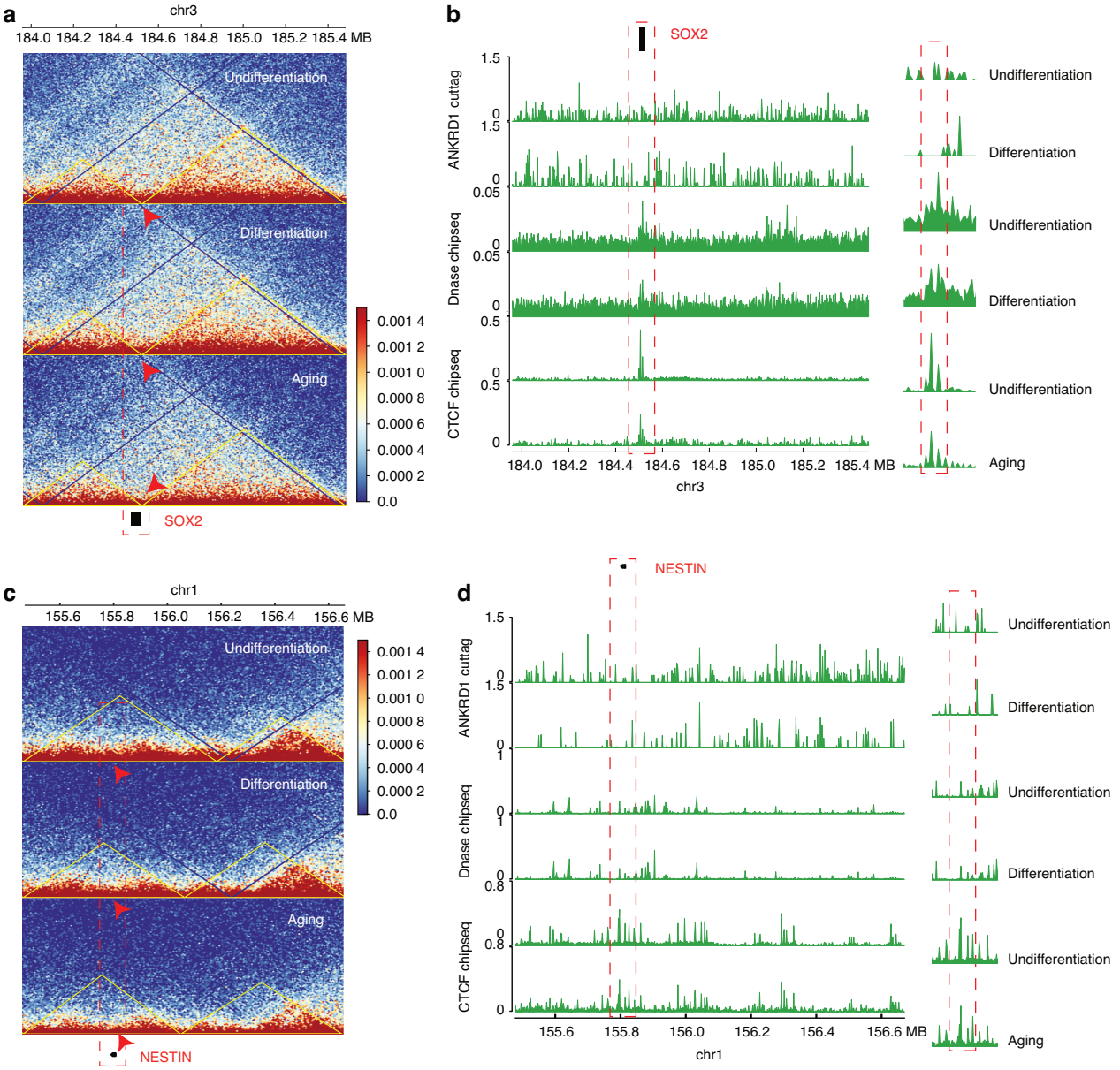

Fig. 5 ANKRD1 sustains divergent chromatin dynamics of SOX2 and NESTIN in BMSCs. **a** Hi-C contact maps for undifferentiated, differentiated and aged BMSCs at SOX2 locus. The Hi-C map displays the chromatin interaction frequencies, with red boxes highlighting the SOX2. The color gradient represents the interaction frequencies, with red indicating higher contact frequencies. **b** Integrative Genomics Viewer (IGV) visualization of ANKRD1 binding and DNase I hypersensitivity at the SOX2 locus in undifferentiated and differentiated BMSCs, along with CTCF signals in undifferentiated and aged BMSCs (green). **c** Hi-C contact maps for undifferentiated, differentiated and aged BMSCs at NESTIN locus. The Hi-C map displays the chromatin interaction frequencies, with red boxes highlighting the NESTIN region. The color gradient represents the interaction frequencies, with red indicating higher contact frequencies. **d** Integrative Genomics Viewer (IGV) visualization of ANKRD1 binding and DNase I hypersensitivity at the NESTIN locus in undifferentiated and differentiated BMSCs, along with CTCF signals in undifferentiated and aged BMSCs (green)

conserved chromatin interactions across differentiation and aging (Fig. 5a). This architectural stability underscores SOX2's role in maintaining genomic organization. In contrast, NESTIN, located within a TAD interior, underwent marked structural remodeling during differentiation and aging, manifested as TAD contraction and weakened intra-domain interactions (Fig. 5c). These alterations profoundly disrupted its regulatory landscape, contributing to reduced expression. Integration of CUT&TAG data with chromatin accessibility (DNase-seq) and insulator (CTCF) signals further illuminated ANKRD1's regulatory influence. At the SOX2 locus, undifferentiated BMSCs displayed robust ANKRD1 occupancy, heightened chromatin accessibility, and strong CTCF binding, whereas differentiation and aging were associated with diminished ANKRD1 signal and reduced openness (Fig. 5b). Analogous patterns were observed at the NESTIN locus (Fig. 5d). Collectively, these findings position ANKRD1 as a critical factor that sustains an open, permissive chromatin state at both SOX2 and NESTIN in undifferentiated BMSCs, thereby preserving a molecular reservoir for neural differentiation potential.

ANKRD1 reverses aging related spatial memory deficits via neuron-targeted overexpression

Next, to investigate the role of ANKRD1 in neurogenic maintenance, we conducted behavioral analyses in natural aging

model mice. Considering the necessity for the virus to cross the blood-brain barrier (BBB) and transduce neuronal cells, we employed an adeno-associated virus (AAV) construct containing the neuron-specific Syn promoter. We systemically delivered either AAV overexpressing ANKRD1 (experimental group, $n = 8$) or control AAV (control group, $n = 8$) via tail vein injection into aged (18-month-old) mice. AAV-mediated expression usually peaked within 4 weeks. Accordingly, we performed animal imaging in vivo after 4 weeks injection to confirm the ANKRD1 expression. Consistent with our expectations, the ANKRD1 signal was predominantly detected in the head, dorsal region, and hindlimbs of the animals (Fig. 6a). Following in vivo imaging, mice underwent behavioral assessments to evaluate neurological functions. Open field testing (OFT) revealed no significant alterations in overall locomotor activity (e.g., total distance traveled, average speed) upon ANKRD1 overexpression mouse (Fig. 6b–d). Similarly, analysis of movement trajectories demonstrated no significant difference between experimental and control groups in either the crossing frequency or time durations in the central zone, the quadrilateral regions, and four-cornered regions (Fig. 6e–h). These data reveal no significant differences in anxiety-like behaviors or motor ability between the two groups.

Next, we performed the Morris water maze (MWM) to assess the spatial learning ability of the mice. Analysis of escape latency during the five-day hidden platform training phase revealed no significant difference in swimming speed between experimental and control groups (Fig. 6i), consistent with our open field results and confirming comparable motor function. Critically, ANKRD1 overexpression in aged mice exhibited significantly shorter latencies to locate the platform versus controls (Fig. 6j). In addition, post-trial analysis revealed superior platform quadrant occupancy and increased platform-crossing frequency in ANKRD1 expression mice (Fig. 6k–m). Collectively, these findings demonstrate that ANKRD1 can rescue age-associated spatial memory deficits, suggesting a protective role against neurocognitive decline in the context of neurodegenerative processes.

To understand how ANKRD1 rescues age-related spatial memory deficits through activation of endogenous BMSCs during nerve repair, we first examined its potential role in promoting neural fate commitment. Overexpression of ANKRD1 in BMSCs led to marked upregulation of key neural lineage markers, including NGFR, SOX10, S100B, NF200, and NeuN (Fig. S5a, b). Immunofluorescence staining further revealed enhanced βIII-tubulin expression accompanied by pronounced morphological changes, including extension of long, filamentous processes characteristic of neuronal cells (Fig. S5c). Additionally, ANKRD1 overexpression also increased the expression and secretion of key neurotrophic factors (NGF, BDNF, GDNF, and FGF2), as confirmed by qRT-PCR, Western blotting, transcriptome profiling and ELISA quantification of culture supernatants (Fig. S5d, g). Collectively, these results demonstrate that ANKRD1 promotes neural fate commitment and augments secretory activity in endogenous BMSCs, thus contributing to the mechanisms of nerve injury recovery.

ANKRD1 mediated neural activation patterns across cognitive-associated brain regions

To further explore the cognitive improvement effect of ANKRD1, we next sought to map its neuroanatomical targets in the mouse brain. c-Fos is expressed in neurons and it provides a cellular method for labeling neurons activated by a variety of stimuli, having widespread application in neurobiological research.[40] Following viral-mediated ANKRD1 overexpression and brain tissue clearing in aged mice, we observed significant increases of c-Fos fluorescence signals within cognition-associated regions including the hippocampal formation (HPF), hypothalamus (HY), and isocortex (Fig. 7a). Quantification of brain-wide activation patterns revealed robust differences in large structures, with the HY, isocortex, HPF, olfactory areas (OLF), striatum (STR), and medulla (MY) showing the most pronounced responses to ANKRD1 overexpression (Fig. 7b). Next, differential activation was further confirmed through z-score and coefficient of variation (CV) analyses, demonstrating both enhanced magnitude (z-score) and greater interindividual variability (CV) in the AAV-ANKRD1 group across multiple regions (Fig. 7c, d).

To delineate the specificity of ANKRD1-mediated neural activation, we conducted a volcano plot analysis of regional c-Fos expression, and we identified five major regions with significantly elevated activation: HY, isocortex, HPF, OLF, and pons (P), along with their subregions (Fig. 7e, f). Given the inherently interconnected nature of neural circuits, we subsequently performed systems-level analysis of functional connectivity using Spearman's rank correlation (ρ) matrices. Positive correlations between brain regions ($0 < \rho < 1$) reflect synchronized or coordinated neural activity, indicative of functional cooperation within neuronal networks. Conversely, negative correlations ($-1 < \rho < 0$) suggest an inverse relationship, where activation in one region is associated with decreased activity in another.[41] In control group, we observed the expected both positive and negative correlation among various brain regions, reflecting normal functional complexity (Fig. 7g). However, AAV-ANKRD1 treatment triggered a pronounced shift toward globally synchronized network states, characterized by significant strengthening of positive correlations across the analyzed brain regions (Fig. 7g). To further investigate ANKRD1's impact on neural circuit engagement, we performed a cross-group correlation analysis of c-Fos fluorescence signal across the 15 anatomically defined brain regions. Notably, 12 of these regions exhibited significantly stronger positive correlations in the AAV-ANKRD1 group compared to AAV-vector controls ($p < 0.05$, FDR-corrected), indicating that ANKRD1 overexpression enhances coordinated activity within these regions (Fig. 7h). These findings demonstrate that ANKRD1 mediate a specific transition from segregated processing toward integrated network states, potentially facilitating functional connectivity by promoting synchronized activation across brain regions.

DISCUSSION

Cranial neural crest-derived mesenchyme plays a pivotal role in craniofacial morphogenesis during embryogenesis. These multipotent cells migrate to encapsulate the anterior neural tube, giving rise to the formation of the meningeal, chondrogenic, and osteogenic lineages that construct the skull and associated connective tissues.[42] Consequently, jaw bone derived from the cranial neural crest exhibits superior physiological responses in developmental, mechanical, and homeostatic contexts compared to other skeletal elements.[43–45] For example, in ovariectomized rats, the jaw bone demonstrates remarkable resilience, with significantly slower loss of trabecular bone volume and mineral density than observed in tibial primary spongiosa.[46] Meanwhile, jaw bone-derived BMSCs functionally diverge from their long-bone counterparts, displaying altered proliferative capacity, life span before senescence, and enhanced osteogenic differentiation potential.[43,47] Unlike their mesoderm-derived counterparts in long bones, jaw-derived BMSCs originate from the neural crest - a transient embryonic cell population renowned for its exceptionally robust neurodevelopmental capacity.[48,49] As a result, given the neural crest origin of jaw-derived BMSCs, a fundamental but understudied question remains: Do jaw bone-derived BMSCs retain ancestral neurogenic functions inherited from their progenitors, unlike mesoderm-derived BMSCs from long bones? In this study, we have compared the features of jaw bone-derived BMSCs in comparison to those derived from other mesodermal origins (rib marrow-derived BMSCs). To explore potential differences, we first compared stemness markers via Western blotting and qPCR. These analyses indicated higher baseline expression of key pluripotency-associated factors (e.g., KLF4, KLF5, SOX2, OCT4,

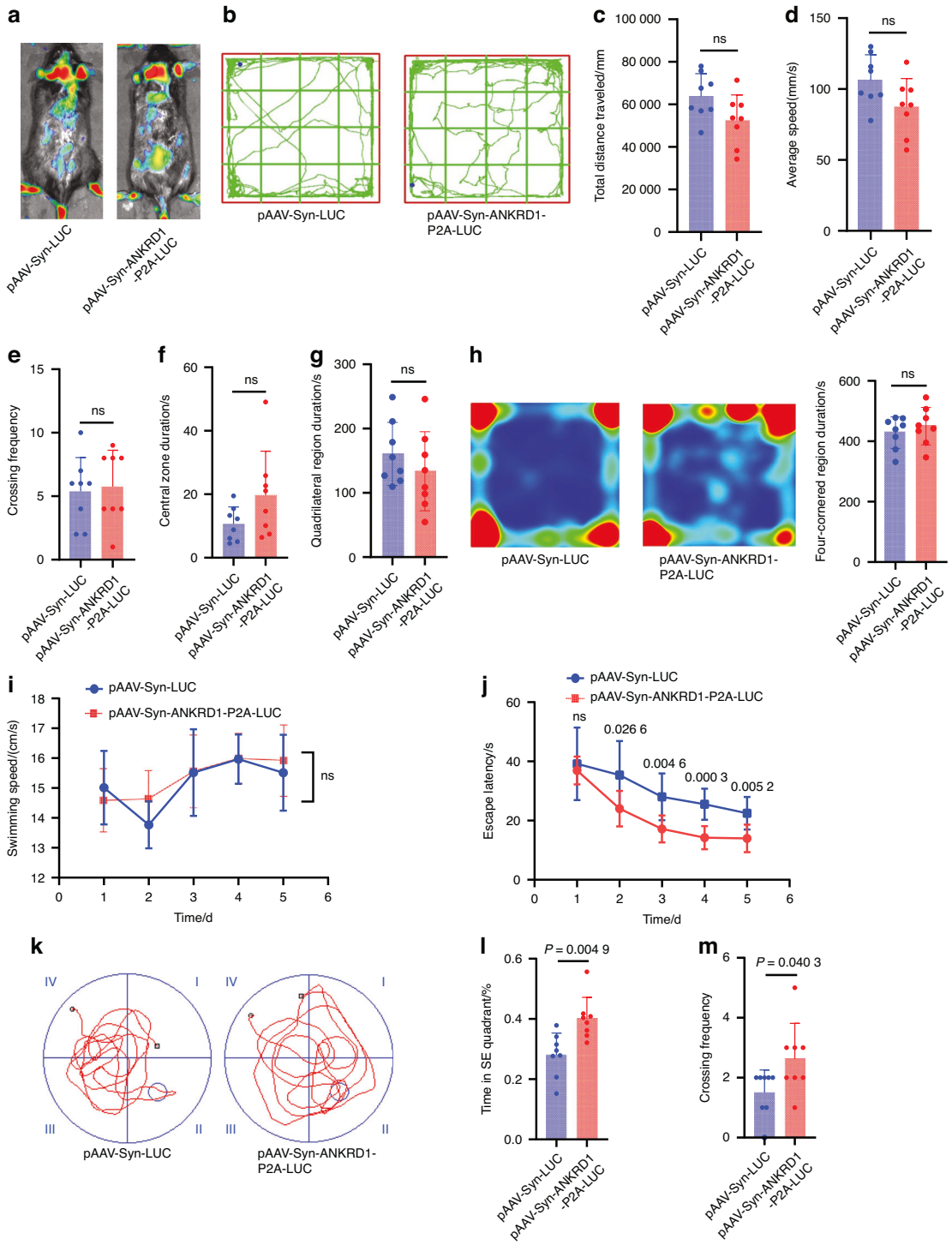

Fig. 6 ANKRD1 reverses aging related spatial memory deficits via neuron-targeted overexpression. **a** Tail vein injection of either pAAV-Syn-ANKRD1-P2A-LUC (experimental, $n = 8$) or pAAV-Syn-LUC (control, $n = 8$) in 18-month-old C57BL/6J mice (2×10^{11} vg per mouse), with bioluminescence imaging (Day 21 post-injection) revealing greater brain signal. **b**–**d** Representative locomotor traces and quantitative statistics (total distance traveled, average speed) of control and ANKRD1-overexpressing mice in the Open field test (OFT). **e**–**g** Quantitative statistics of crossing frequency, central zone duration and quadrilateral region duration of control and ANKRD1-overexpressing mice in the OFT. **h** Representative open field exploration heatmap and quantitative analysis of duration in corner zones showing no significant corner preference in ANKRD1 overexpression mice versus controls. **i** Quantitative statistics of average swimming speed of control and ANKRD1-overexpressing mice in the Morris water maze experiment. **j** Quantification of average time to locate the hidden platform across training days for control versus ANKRD1-overexpressin mice. **k** Representative locomotor traces of control and ANKRD1-overexpressing mice in the Morris water maze experiment. **l** Percentage of time spent in the second quadrant by control and ANKRD1-overexpressing mice during the MWM. **m** Quantification of the number of crossings over the hidden platform location during training days for control and ANKRD1-overexpressing mice

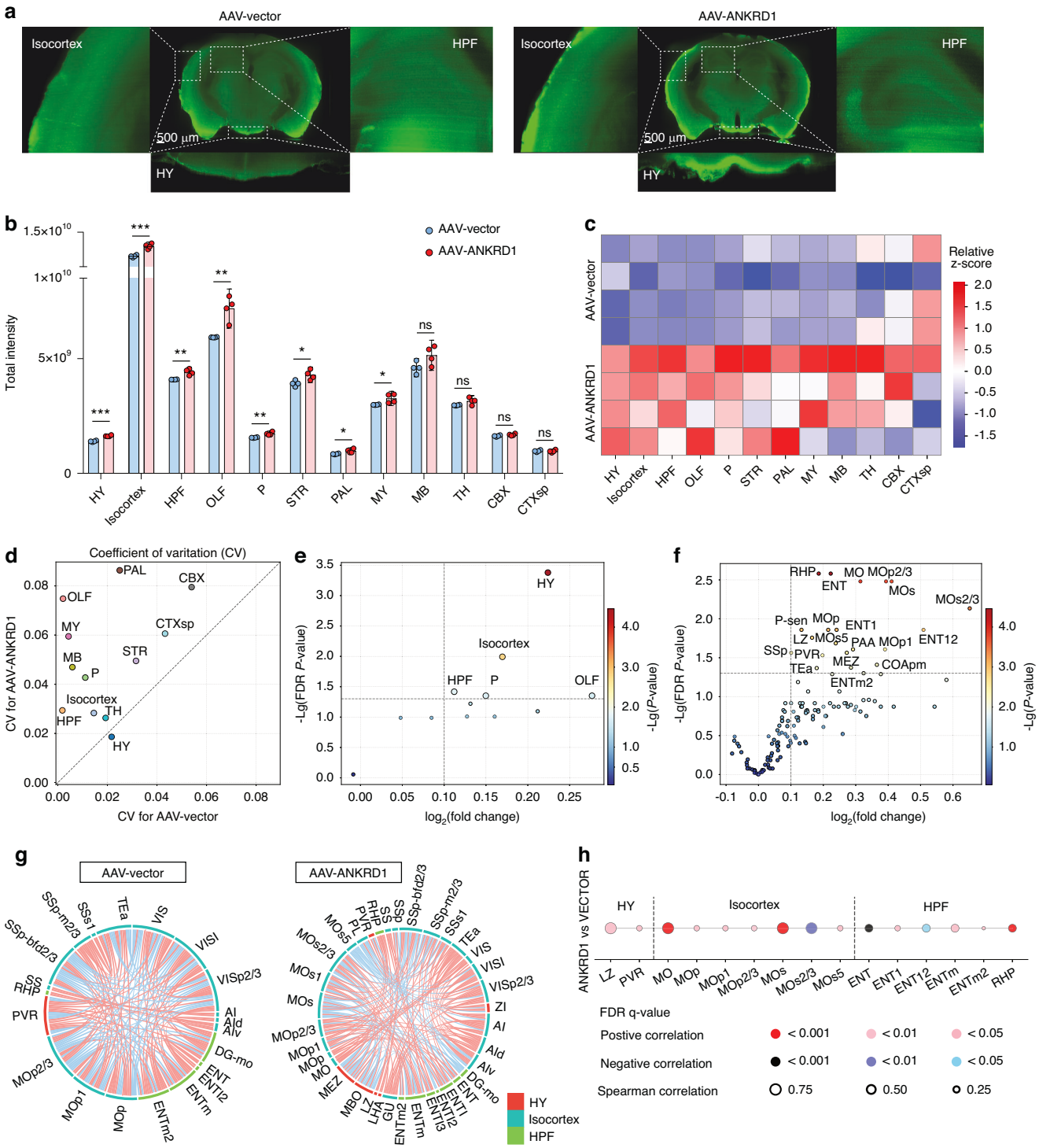

Fig. 7 ANKRD1 mediated neural activation patterns across cognitive-associated brain regions. **a** Virtual coronal sections showing c-Fos expression patterns in AAV-vector (left) and AAV-ANKRD1 (right) groups. Cognition-associated regions (HP, HY, isocortex) were included. Scale bar, 500 μm. **b** Whole-brain c-Fos fluorescence signal in AAV-vector and AAV-ANKRD1 groups. $^{*}P < 0.05$; $^{**}P < 0.01$; $^{***}P < 0.001$. **c** Relative z -score plot of 12 brain areas of 8 animals from two groups. **d** Coefficient variation plot of 12 brain areas between the control and ANKRD1 overexpression group. **e**, **f** Comparison of differential neuronal activation by control and ANKRD1 overexpression. The vertical line represents the fold change in c-Fos fluorescence signal >1.07, and the horizontal line represents the FDR *P*-value of 0.05. The color of the dots represents the level of the FDR *P*-value. **g** The correlation of c-Fos fluorescence signal in AAV-vector and AAV-ANKRD1 groups across HY, isocortex, HPF, OLF, and pons areas. The red lines represent positive correlation and the blue lines indicate negative correlation. **h** Spearman correlation analysis of c-Fos fluorescence signals across 15 brain regions between the AAV-vector control and AAV-ANKRD1 groups. The size of each bubble corresponds to the magnitude of the correlation levels, and the color gradient represents FDR *q*-values. Red denotes positive correlation and blue indicates negative correlation

and NANOG) in jaw bone-derived BMSCs relative to their mesodermal counterparts (Fig. S6a, b). We then assessed their ability to differentiate into neural cells by subjecting both cell types to neural induction using a standard NSC culture medium. While mesodermal BMSCs showed only limited upregulation of neuronal markers (including NeuN, NF200, NGFR, SOX10, and S100B) following induction, jaw bone-derived BMSCs exhibited a much more pronounced increase in these markers (Fig. S6c). Under microscopy, the latter cells also developed evident neuronal-like features, such as elongated processes and enhanced synaptic extensions, whereas morphological changes in mesodermal BMSCs were considerably less apparent (Fig. S6d). Furthermore, immunofluorescence staining for the early neuronal marker βIII-tubulin corroborated these findings: jaw bone-derived BMSCs displayed a substantial elevation in βIII-tubulin signal and clear neuronal morphological transformation post-induction, in contrast to the milder responses observed in mesodermal BMSCs (Fig. S6e). These observations are consistent with the unique embryonic origin of jaw bone-derived BMSCs from the neural crest (ectodermal-derived), as opposed to the purely mesodermal lineage of conventional BMSCs.

The ANKRD (Ankyrin Repeat Domain) protein family, characterized by the presence of Ankyrin Repeat (AR) motifs that mediate specific protein-protein interactions, constitutes an evolutionarily conserved group of eukaryotic regulatory factors.[50–52] ANKRD members serve as molecular scaffolds and signaling hubs that orchestrate diverse cellular processes, ranging from signal transduction and cytoskeletal organization to transcriptional regulation and apoptosis.[22,53–55] Emerging evidence indicates that the ANKRD family critically regulates embryonic differentiation and neural crest development. For instance, ANKRD11 knockout mice exhibit severe neurodevelopmental defects and craniofacial malformations, phenocopying KBG syndrome in humans—a neurodevelopmental disorder caused by heterozygous ANKRD11 mutations.[56,57] Studies have shown that conditional knockout of ANKRD11 in mouse embryonic NCCs leads to impaired expression of various transcription factors, chromatin remodelers, and signaling pathway components, including the mTOR, BMP, and TGF-β pathways, in cardiac NCCs.[58] Mechanistically, structural analyses revealed that ANKRD11 mutation (Tyr347Ala) selectively impairs cohesion binding, leading to widespread gene expression dysregulation in ESCs.[59] Furthermore, ANKRD11 enhances the transcriptional activity of p53 by promoting its acetylation, thereby expanding its regulatory scope beyond classical tumor suppression.[60–62]

Increasing evidence indicates that stem cell lineage commitment is orchestrated by complex interplay between epigenetic modifications and three-dimensional (3D) genome organization.[63] During BMSC differentiation and aging, chromatin spatial architecture undergoes extensive remodeling, accompanied by weakened interactions between regulatory elements and genes involved in protein synthesis, ultimately culminating in cellular senescence.[64] In this study, we identified ANKRD1 as a pivotal regulator of latent neurogenic potential in cranial neural crest-derived BMSCs, establishing a direct link between developmental ontogeny and adult neural plasticity. We demonstrate that jaw bone-derived BMSCs retain a neuroepigenetic signature, orchestrated by ANKRD1 through its governance of super-enhancer networks at neural stemness loci, such as SOX2 and NESTIN. Besides, ANKRD1 maintains an open chromatin architecture and promotes three-dimensional enhancer-promoter interactions, preserving the neurogenic programs in a transcriptionally poised state. This chromatin-level priming not only safeguards neurogenic competence but also reflects a persistent epigenetic imprint of neural crest origin. Intriguingly, beyond its role in chromatin topology, ANKRD1 is also shown being act as a transcriptional modulator, which can bond to P53 tumor suppressor protein and enhances its transcriptional activity.[65] By concurrently orchestrating epigenetic and transcriptional regulation, ANKRD1 emerges as a mechanistic linchpin that bridges transcriptional memory with neurofunctional fidelity.

Cognitive aging, characterized by declining spatial memory and learning capacity, poses a growing socioeconomic challenge in aging populations worldwide.[66,67] At the cellular level, this cognitive decline correlates with diminished neurogenesis, attenuated neural plasticity and synaptic alterations in hippocampal and cortical regions.[68–70] Recently, research has found that neurodegenerative diseases are closely related to protein imbalance.[71] It found that the nuclear receptor NR4A1, a member of nuclear receptor subfamily 4 group A (Nr4a), governs age-related cognitive decline. Human peripheral blood mononuclear cells (PBMCs) exhibit progressive NR4A1 mRNA reduction with aging. In mice model, hippocampal CA1 Nr4a1 levels correlate positively with cognitive performance and Nr4a1 overexpression significantly rescues cognitive deficits in aged mice.[72] Traditionally, jaw bone-derived BMSCs have been recognized primarily for their prominent osteogenic properties and their essential role in maintaining alveolar bone homeostasis.[73–75] However, their potential contribution to neural repair has remained largely unexplored. In this study, we uncover a neurogenic capacity in jaw bone-derived BMSCs, driven by the stemness maintenance factor ANKRD1. We demonstrate that ANKRD1 exhibits remarkable potential to promote neural development and differentiation. Notably, the age-dependent decline in ANKRD1 expression parallels the erosion of cognitive neural networks, whereas targeted therapeutic delivery of ANKRD1 effectively rescues these deficits, highlighting promising avenues for neural rejuvenation strategies. Furthermore, functional connectivity analyses reveal that ANKRD1 orchestrates balanced activation patterns across cognition-related brain regions, particularly the HY, isocortex, HPF, OLF, and P. These findings position ANKRD1 as a key mediator linking peripheral stem cell dynamics in the jaw bone to central nervous system resilience and cognitive health.

Overall, these findings fundamentally advance our understanding of how developmental lineage commitments influence adult tissue homeostasis and age-related functional decline. They also open new avenues for treating cognitive disorders by targeting the ANKRD1-mediated interface between epigenetic memory and neural plasticity.

MATERIALS AND METHODS

Cell culture conditions

All cells used in this study were cultured in a sterile incubator maintained at 37 °C under 5% CO_2 atmosphere. BMSCs from human sources were cultured in low-glucose MEM Alpha complete medium supplemented with 10%–15% fetal bovine serum (FBS) and 1%–2% penicillin-streptomycin. HEK293T cells were cultured in high-glucose DMEM base medium with identical supplementation and incubation conditions. Cell-related procedures–including resuscitation, passaging, cryopreservation, and isolation—were performed under sterile conditions in a biosafety cabinet.

BMSCs isolation from human jaw bone tissue

Sample Acquisition: jaw bone fragments extracted from dental sockets (donor ages: 26–33 years or 66–78 years with informed consent) were immediately immersed in PBS on ice and transferred to the lab within 2 h. Tissue Processing: washing bone samples 3–5 times with PBS containing gradient antibiotic concentrations (5% → 2% → 1% penicillin-streptomycin-amphotericin B). Then mincing the tissue thoroughly with sterile scissors and plated fragments evenly across T25 flask surface. Primary Culture: adding 2 mL complete medium to flask. Incubating under standard conditions (5% CO_2, 37 °C) for 8–10 h without disturbance to enable attachment. After that, carefully adding 4 mL fresh medium along flask wall to prevent dislodging tissue. Maintained culture without medium change for 5 days. Cell Growth Monitoring: spindle-shaped BMSCs typically migrated

from explants after 5 days. Performed first medium change upon visible cell migration. Expansion: Passaged at 7–10 days when high-density colonies formed (80% confluence area) and re-plated original tissue fragments in new flasks for secondary cell outgrowth. Cryopreserved surplus BMSCs in liquid nitrogen for downstream assays.

Transient transfection

Prior to transfection, plasmid DNA was extracted from *E. coli* using commercial kits with confirmed concentration and purity. BMSCs were plated according to growth kinetics and transfected at 60%–70% confluence. For transfection in small culture dishes, 5 μg plasmid was diluted in 300 μL Opti-MEM medium, while 6 μL Lipofectamine 2 000 was separately diluted in 300 μL Opti-MEM. After 5-min incubation for homogeneous mixing (avoiding bubble formation), both solutions were gently combined and incubated for an additional 15 min. The transfection complex mixture was then added dropwise to cells. Following 6–8 h incubation, the medium was replaced. Exogenous gene expression became detectable at 24 h, peaked at 48 h for mRNA and 72 h for protein.

Total RNA extraction

Total RNA was isolated from adherent BMSCs using TRIzol reagent. Cells in small dishes were lysed with 500 μL TRIzol and scraped, followed by 15-min incubation on ice. After adding 100 μL chloroform, samples were mixed by inversion and incubated at room temperature for 3 min to facilitate phase separation. Following centrifugation at 12 000 r/min for 15 min at 4 °C (pre-cooled), the aqueous upper phase was transferred to RNase-free tubes. An equal volume of isopropanol was added, mixed thoroughly, and incubated at −20 °C for 15 min. Subsequent centrifugation at 12 000 r/min for 10 min at 4 °C yielded a white RNA pellet. The pellet was washed with 500 μL 75% ethanol (prepared in DEPC-treated water), then centrifuged at 7 500 r/min for 5 min at 4 °C. Residual liquid was carefully removed with a pipette before briefly drying the transparent pellet in a 65 °C metal bath for 10–15 s. RNA was dissolved in 20 μL pre-heated (65 °C) DEPC-treated water, with concentration and purity measured by spectrophotometry.

Reverse transcription (RT)

RT reactions were performed using Vazyme reverse transcriptase in 10 μL reaction volumes containing 500 ng total RNA. The reaction mix comprised RNA template, 2 μL RT enzyme, and DEPC-treated water (for volume adjustment). After gentle mixing (avoiding bubbles), reactions were run in a thermal cycler under these conditions: 37 °C for 15 min (reverse transcription) followed by 85 °C for 5 s (enzyme inactivation). Synthesized cDNA was stored at −20 °C for subsequent analysis.

Quantitative real-time PCR (qRT-PCR)

A 10-fold dilution of cDNA template was prepared using 90 μL ddH_2O to minimize reverse transcription reagent interference. Primer pairs (forward/reverse) were mixed at 1:1 ratio. Each 20 μL reaction contained: 10 μL 2× AceQ™ qPCR SYBR Green Master Mix, 1 μL pooled primers, and 9 μL diluted cDNA template. Plates were briefly centrifuged to settle components. Then, the corresponding qPCR program was subsequently set up and initiated on the thermal cycler.

Western blotting

Protein samples were separated on 4%–20% gradient gels (70 V stacking → 110 V resolving gel), then transferred to methanol-activated PVDF membranes (200 mA constant current, 120 min), and validated by Ponceau S staining. After that, membranes were blocked in 5% milk/TBS-T, incubated with primary antibody (4 °C overnight) and species-matched HRP-conjugated secondary (1:10 000, 60 min), then detected by ECL Prime substrate.

Osteogenic induction and alizarin red staining

Gelatin-coated 6-well plates were seeded with P3 BMSCs (2×10^5 cells per well) in growth medium (DMEM + 10% FBS). At 50%–60% confluency, medium was replaced with osteogenic induction medium containing: DMEM; 10% FBS; 50 μg/mL ascorbic acid (Sigma A4544);10 mmol/L β-glycerophosphate (Sigma G9422); 100 nmol/L dexamethasone (Sigma D4902). Cells were maintained for 21 days (37 °C, 5% CO_2, 95% humidity) with medium changes every 72 h. Untreated controls received standard growth medium. Post-induction: wash cells ×1 with PBS, then fixing in chilled 4% PFA (30 min, RT), washing ×3 with dd H_2O. After that, staining with 500 μL of 2% Alizarin Red S (pH 4.2, Millipore TMS008) for 30 min (RT, dark), then washing ×3 with distilled water. Quantify mineralized nodules by microscopic.

Adipogenic induction and modified oil red O staining

BMSCs (2×10^5 cells/well) were maintained similarly as in osteogenic induction. At 60%–70% confluency, adipogenic induction was initiated using adipogenic cocktail: DMEM/F12;10% FBS; 0.5 mmol/L IBMX (Sigma I7018); 10 μmol/L insulin (Sigma I0516); 1 μmol/L dexamethasone; 200 μmol/L indomethacin (Sigma I7378). Cells were cultured for 21 days (37 °C, 5% CO_2) with medium changes every 48 h. Post-induction: washing ×1 with PBS, then fixing in precooled 4% PFA (10 min, RT). After that, washing ×2 with PBS. Then incubating with 60% isopropanol (20 s), Staining with modified Oil Red O working solution (0.3% w/v in 60% isopropanol, filtered through 0.22 μm) for 15 min (RT, dark). Then destaining with 60% isopropanol (30 s), washing ×1 with PBS (20 s). Quantify lipid accumulation by image analysis.

Cell immunofluorescence (IF)

Cell Seeding: Cells were seeded onto sterile glass coverslips (12 mm diameter; #1.5 thickness) placed in 24-well plates. Briefly, cells were resuspended in pre-warmed culture medium, added to wells, and allowed to adhere overnight (37 °C, 5% CO_2). Optimal cell density ($\approx 10^4$–10^5 cells per well) was confirmed by microscopy prior to fixation. Fixation: Medium was aspirated and cells washed twice gently with RNase-free DPBS (Ca^{2+}/Mg^{2+}-free). Cells were fixed with freshly prepared 4% paraformaldehyde (PFA) in DEPC-treated PBS for 20 min at room temperature (RT). Permeabilization: After three DPBS washes, cells were permeabilized with 0.5% Triton X-100 in DPBS (400 μL per well) for 15 min at RT. Blocking: Permeabilization solution was aspirated and non-specific sites blocked with 5% bovine serum albumin (BSA) in DPBS (400 μL per well, 1 h, RT). Primary Antibody Incubation: Primary antibodies were diluted in IF antibody dilution buffer according to manufacturer recommendations. Blocking solution was removed, cells washed 3× with DPBS, and 200 μL diluted primary antibody solution added per well (overnight, 4 °C). Washing: Primary antibody solution was aspirated. Cells were washed 3× (8 min per wash, 100 rpm orbital shaking) with PBST (DPBS + 0.05% Tween-20). Secondary Antibody Incubation: Species-matched fluorophore-conjugated secondary antibodies diluted in IF antibody buffer were added (200 μL per well; 1 h, RT, dark). Washing: Secondary antibody was aspirated. Cells washed 3× with PBST. Nuclear Counterstaining & Mounting: Cells were incubated with DAPI (1 μg/mL in DPBS, 4 min, dark), washed 3× with DPBS, and coverslips mounted on glass slide. Confocal microscopy (Carl Zeiss, LSM980) was performed within 48 h.

CUT&Tag (Cleavage under targets & tagmentation)

The CUT&Tag assay was performed using the Hyperactive Universal CUT&Tag Assay Kit for Illumina Pro (Vazyme) according to the manufacturer's instructions with minor modifications. Briefly, ConA Beads Pro were activated in Binding Buffer, washed twice, and resuspended. Approximately $(5–10) \times 10^4$ cells were harvested, washed in PBS, and bound to the activated beads by gentle rotation at room temperature. After incubation, bead-bound cells were resuspended in Antibody Buffer containing primary

antibodies and incubated overnight at 4 °C. The next day, cells were washed and incubated with secondary antibody (1:100 dilution in Dig-wash Buffer) for 30–60 min at room temperature. Following two washes in Dig-wash Buffer, cells were resuspended in Dig-300 Buffer containing pA/G-Tnp Pro and incubated for 1 h at room temperature. After two additional washes in Dig-300 Buffer, tagmentation was performed by resuspending the beads in 5× TTBL supplemented with Dig-300 Buffer and incubating at 37 °C for 60 min. Reactions were stopped by adding 10% SDS and DNA Spike-in, followed by incubation at 55 °C to release tagmented DNA. Fragmented DNA was purified using DNA Extract Beads Pro with B&W Buffer washes. Purified DNA was amplified by PCR (9–12 cycles) using index primers (N5XX/N7XX series) and CAM master mix. Amplified libraries were purified twice with VAHTS DNA Clean Beads, eluted in ddH_2O, and subjected to quality control before Illumina sequencing.

Dual-luciferase reporter assay

The dual-luciferase reporter system quantifies transcriptional regulatory activity by measuring the Firefly luciferase (FLuc) to Renilla luciferase (RLuc) luminescence ratio, with RLuc serving as an internal control for normalization. To validate ANKRD1-mediated transcriptional regulation of SOX2 and NESTIN, genomic regions containing predicted enhancers and promoters (identified by CUT&Tag data) were synthesized (Genewiz Inc.) and cloned upstream of the FLuc gene in the pGL4.23[luc2/minP] vector. Cells were transfected at 60–70% confluence. For 24-well plates, 500 ng total DNA was transfected per well using a plasmid ratio of 25:25:1 (ANKRD1 overexpression plasmid: SOX2/NESTIN-enhancer/promoter-pGL4.23: pRL-SV40 Renilla control plasmid). After 8 h, transfection medium was replaced with fresh growth medium. At 36 h post-transfection, cells were washed twice with PBS and lysed in 1× Passive Lysis Buffer (Promega) with agitation (10–15 min, RT). Lysates were clarified by centrifugation (10 min, 1 200 × *g*, 4 °C). FLuc and RLuc assay substrates were prepared from the Luc-Pair™ Duo-Luciferase HS Assay Kit (GeneCopoeia) per manufacturer instructions and protected from light. Twenty microliters lysate aliquot was mixed with 10 µL FLuc substrate, vortexed briefly (3–4 s), and luminescence measured immediately (integration: 2–10 s). 10 µL RLuc substrate was then added to the same tube, vortexed, and RLuc luminescence recorded. Transcriptional activity was calculated as normalized FLuc/RLuc ratio. Elevated ratios indicate enhanced SOX2 and NESTIN promoter/enhancer activity induced by ANKRD1.

AAV tail vein injection

AAV preparation: AAV-Syn-ANKRD1 or AAV-Syn-Empty control was diluted in sterile PBS to 2×10^{11} vg per mouse (total volume: 100–200 µL). Aliquots stored at −80 °C. Mice were restrained in an injector device with tails immobilized. Tail veins were dilated by immersion in warm water (37 °C, 30–60 s). Virus solution was injected slowly into the lateral tail vein using a 29G insulin syringe. Viral titers and injection volumes were matched between groups. Post-injection, mice were monitored daily for 48 h and ≥2× per week thereafter. Experiments commenced 4 weeks post-injection to ensure peak transgene expression.

In vivo bioluminescence imaging

Substrate preparation: D-Luciferin potassium salt (GoldBio) was dissolved in calcium/magnesium-free D-PBS to 15 mg/mL, sterile-filtered (0.22 µm), aliquoted, and stored at −20 °C. Imaging protocol: Mice received intraperitoneal D-luciferin (150 mg/kg, 10 µL/g body weight). Imaging commenced 12 min post-injection under isoflurane anesthesia (induction: 3%–4%; maintenance: 1.5%–2.5% in O_2). Data acquisition: Bioluminescence was quantified using an IVIS Spectrum (PerkinElmer). Signal intensity was analyzed with Living Image® Software.

Open field test (OFT)

Animals were habituated to the testing room for 3–4 days prior to experiments. Thirty minutes before testing, mice were placed in a quiet holding area to acclimate. Testing occurred in a $50 \times 50 \times 40$ cm^3 open field arena, demarcated into a central zone and a peripheral zone. Each mouse was placed in the center of the arena and allowed to explore freely for 10 min. Behavior was recorded by an automated tracking system configured to divide the arena into 16 virtual grid squares (central zone: 4 center squares). Parameters quantified included: (1) Total distance traveled; (2) Distance traveled in the central zone; (3) Ratio of peripheral distance to total distance; (4) Time spent in the central zone. Then, the arena surface was cleaned with 70% ethanol between subjects to remove olfactory cues. A single experimenter performed all tests and recordings to ensure consistency.

Morris water maze (MWM)

Mice were acclimated to the water maze testing room under a controlled light/dark cycle (12 h/12 h) for 1–2 days prior to testing. Experiments were conducted in a quiet environment maintained at optimal temperature (22 °C ± 1 °C) and humidity (55%± 5%). Testing occurred in a circular pool (150 cm diameter, 80 cm height) filled with water (25 °C ± 1 °C) rendered opaque using titanium dioxide (TiO_2) powder to facilitate tracking of black-furred mice. Distinct visual cues were placed on the pool walls at the midpoint of each quadrant. Visible Platform Training (Day 1): A platform (10 cm diameter) was positioned 1 cm above the water surface at the center of two diagonally opposite quadrants. Mice underwent four trials per day (inter-trial interval: ≥15 min), released consecutively from pseudorandomly selected start points at the quadrant peripheries. Each trial lasted up to 60 s. If a mouse failed to find the platform within 60 s, it was gently guided to the platform and allowed to remain there for 15 s. Mice were immediately dried after each trial. Mean escape latency and swimming speed across the 4 trials were analyzed. Hidden Platform Acquisition (Days 2–6): The platform was submerged ≈1 cm below the water surface and remained fixed in the center of Quadrant II. Mice underwent four daily trials from pseudo-randomly varied start points at the periphery of each quadrant. Escape latency across the 5 days was recorded. Mice were dried promptly after each trial. Probe Test (Day 7): The platform was removed. Mice were released from the quadrant most distal to the former platform location (in Quadrant II) and allowed to swim for 60 s. Parameters analyzed included: (1) Time spent in the target quadrant (Quadrant II); (2) Distance traveled in the target quadrant; (3) Number of platform location crossings.

Whole-brain immunostaining and tissue clearing

Mice were anesthetized and transcardially perfused. Perfusion began with ≈30 mL room-temperature 1× PBS, followed immediately by 5–10 min perfusion with ice-cold 4% paraformaldehyde (PFA) until blood clearance was confirmed by liver blanching. Brains were post-fixed in 4% PFA at 4 °C overnight. Fixed brains underwent sequential delipidation and decolorization steps based clearing kit manufacturer's protocol. Brains were then rehydrated in 1× PBS at RT (3 × 20 min) followed by overnight blocking at RT in blocking solution (1× Casein buffer containing 0.5% NP-40 and 10% DMSO). Primary antibodies (diluted 1:100 in blocking solution) were applied, and brains were incubated for 3 days at 4 °C with gentle agitation. After primary incubation, brains were washed with 1× PBS at RT (≥3 washes over 24 h). Corresponding secondary antibodies (diluted 1:100 in blocking solution) were applied and incubated under identical conditions for 3 days, followed by washing in 1× PBS at RT (≥3 washes over 12 h). Samples were dehydrated in graded clearing solution at 37 °C with gentle agitation for 2 days (solution refreshed daily). Trace dehydration reagent was removed from tissues using absorbent paper, followed by incubation in PEGASOS Solution until optically clear (≈2 days for aged mouse brains). Cleared brains could be

imaged immediately or stored long-term at 4 °C in PEGASOS Solution, wrapped in aluminum foil. The analysis of c-Fos signal intensity consisted of following steps: For registration to the Allen CCFv3 atlas, an initial automated alignment was performed using the registration module of VISoR Suite software (Bineogen Tech), followed by manual refinements in Freesia (https://github.com/dinglufe/freesia-atlas-cell-counting). The voxel coordinates were then transformed into the Allen CCFv3 reference space to quantify the total c-Fos signal intensity for each brain region. Image generation and statistical analyses were conducted using Lychnis (https://github.com/dinglufe/Lychnis-tracing) alongside the statistical analysis module of VISoR Suite software.

Data analysis

Data are presented as mean ± standard deviation (SD). All experiments consisted of at least three independent biological replicates. Statistical analyses were performed using GraphPad Prism (version 9.0). Comparisons between two groups utilized unpaired two-tailed Student's *t*-tests. A probability value (*P*) of <0.05 was considered statistically significant.

Ethical approval and consent to participate

The study design, protocol and informed consent were approved and adopted by the Ethical Committee at Anhui Medical University and the College & Hospital of Stomatology of Anhui Medical University. The project "Collecting jaw bone fragments during dental implant surgery to prepare primary human bone marrow mesenchymal stem cells" was approved on October 20, 2021 with approval number of T2021014. Animal experiments were approved by the Laboratory Animal Care and Use Committee of Anhui Medical University (Approval No. LLSC202522135) and were performed in accordance with institutional guidelines.

DATA AVAILABILITY

Data used and/or analyzed are available from the corresponding author upon reasonable request.

ACKNOWLEDGEMENTS

We thanks for the support of Center for Scientific Research, Anhui Medical University. We acknowledge OmicShare tools for bioinformatics analysis.

AUTHOR CONTRIBUTIONS

Software, Investigation, Writing—original draft preparation: Zifei Wang, Xiaoyun Liu, Wenyu Zhen, Writing—review and editing: Hengguo Zhang, Fei Xu, Rui Wang, Wenhu Fan, Methodology, Software, Visualization, Investigation: Wenhao Zhang, Yulong Zhang, Visualization, Supervision: Wansu Sun, Mingyue Wu, Conceptualization, Funding acquisition: Jiacai He, Hao Gu, Hengguo Zhang. All the authors read and approved the final manuscript.

FUNDING

This research was supported by grants from the open research project of State Key Laboratory of Oral Diseases (no. SKLOD2024OF03), the Anhui Province Outstanding Young Teachers Development Program (no. YQYB2024013), and the National Natural Science Foundation of China (nos. 82201026 and 82571071).

ADDITIONAL INFORMATION

Supplementary information The online version contains supplementary material available at https://doi.org/10.1038/s41368-026-00428-5.

Competing interests: The authors declare that the research was conducted in the absence of any commercial or financial relationships that could be construed as potential conflicts of interest.

Consent for publication: We promise to agree to publish our article in this journal.

REFERENCES

1. Menendez, L. et al. Directed differentiation of human pluripotent cells to neural crest stem cells. *Nat. Protoc.* **8**, 203–212 (2013).
2. Lee, G., Chambers, S. M., Tomishima, M. J. & Studer, L. Derivation of neural crest cells from human pluripotent stem cells. *Nat. Protoc.* **5**, 688–701 (2010).
3. Martik, M. L. & Bronner, M. E. Riding the crest to get a head: neural crest evolution in vertebrates. *Nat. Rev. Neurosci.* **22**, 616–626 (2021).
4. Changmeng, Z., Hongfei, W., Cheung, M. C., Chan, Y. S. & Shea, G. K. Revealing the developmental origin and lineage predilection of neural progenitors within human bone marrow via single-cell analysis: implications for regenerative medicine. *Genome Med.* **15**, 66 (2023).
5. Romero-Ramírez, L. et al. Treatment of rats with spinal cord injury using human bone marrow-derived stromal cells prepared by negative selection. *J. Biomed. Sci.* **27**, 35 (2020).
6. Xu, Y. et al. USP26 combats age-related declines in self-renewal and multipotent differentiation of BMSC by maintaining mitochondrial homeostasis. *Adv. Sci.* **11**, e2406428 (2024).
7. Han, D. et al. Multipotent neural stem cells originating from neuroepithelium exist outside the mouse central nervous system. *Nat. Cell Biol.* **27**, 605–618 (2025).
8. Miyagi, S. et al. The Sox2 regulatory region 2 functions as a neural stem cell-specific enhancer in the telencephalon. *J. Biol. Chem.* **281**, 13374–13381 (2006).
9. Reynolds, B. A. & Weiss, S. Generation of neurons and astrocytes from isolated cells of the adult mammalian central nervous system. *Science* **255**, 1707–1710 (1992).
10. Episkopou, V. SOX2 functions in adult neural stem cells. *Trends Neurosci.* **28**, 219–221 (2005).
11. Thomson, M. et al. Pluripotency factors in embryonic stem cells regulate differentiation into germ layers. *Cell* **145**, 875–889 (2011).
12. Zhou, H. Y. et al. A Sox2 distal enhancer cluster regulates embryonic stem cell differentiation potential. *Genes Dev.* **28**, 2699–2711 (2014).
13. Chakraborty, S. et al. Enhancer-promoter interactions can bypass CTCF-mediated boundaries and contribute to phenotypic robustness. *Nat. Genet.* **55**, 280–290 (2023).
14. Bonev, B. et al. Multiscale 3D genome rewiring during mouse neural development. *Cell* **171**, 557–572.e524 (2017).
15. Uchikawa, M., Ishida, Y., Takemoto, T., Kamachi, Y. & Kondoh, H. Functional analysis of chicken Sox2 enhancers highlights an array of diverse regulatory elements that are conserved in mammals. *Dev. Cell* **4**, 509–519 (2003).
16. Taylor, T. et al. Transcriptional regulation and chromatin architecture maintenance are decoupled functions at the Sox2 locus. *Genes Dev.* **36**, 699–717 (2022).
17. Jin, Z. et al. Different transcription factors regulate nestin gene expression during P19 cell neural differentiation and central nervous system development. *J. Biol. Chem.* **284**, 8160–8173 (2009).
18. Zimmerman, L. et al. Independent regulatory elements in the nestin gene direct transgene expression to neural stem cells or muscle precursors. *Neuron* **12**, 11–24 (1994).
19. Johansson, C. B., Lothian, C., Molin, M., Okano, H. & Lendahl, U. Nestin enhancer requirements for expression in normal and injured adult CNS. *J. Neurosci. Res.* **69**, 784–794 (2002).
20. Chen, Y. et al. Super-enhancer-driven IRF2BP2 enhances ALK activity and promotes neuroblastoma cell proliferation. *Neuro Oncol.* **26**, 1878–1894 (2024).
21. Benabdallah, N. S. et al. Decreased enhancer-promoter proximity accompanying enhancer activation. *Mol. Cell* **76**, 473–484.e477 (2019).
22. Xu, X. et al. Research progress of ankyrin repeat domain 1 protein: an updated review. *Cell Mol. Biol. Lett.* **29**, 131 (2024).
23. Moulik, M. et al. ANKRD1, the gene encoding cardiac ankyrin repeat protein, is a novel dilated cardiomyopathy gene. *J. Am. Coll. Cardiol.* **54**, 325–333 (2009).
24. Xie, R. et al. Nuclear AGO2 promotes myocardial remodeling by activating ANKRD1 transcription in failing hearts. *Mol. Ther.* **32**, 1578–1594 (2024).
25. Piroddi, N. et al. Myocardial overexpression of ANKRD1 causes sinus venosus defects and progressive diastolic dysfunction. *Cardiovasc. Res.* **116**, 1458–1472 (2020).
26. Murphy, N. P., Lubbers, E. R. & Mohler, P. J. Advancing our understanding of AnkRD1 in cardiac development and disease. *Cardiovasc. Res.* **116**, 1402–1404 (2020).
27. Samaras, S. E., Almodóvar-García, K., Wu, N., Yu, F. & Davidson, J. M. Global deletion of Ankrd1 results in a wound-healing phenotype associated with dermal fibroblast dysfunction. *Am. J. Pathol.* **185**, 96–109 (2015).
28. Zhang, Q. et al. Down-regulating scar formation by microneedles directly via a mechanical communication pathway. *ACS Nano* **16**, 10163–10178 (2022).

29. Lei, Y., Henderson, B. R., Emmanuel, C., Harnett, P. R. & deFazio, A. Inhibition of ANKRD1 sensitizes human ovarian cancer cells to endoplasmic reticulum stress-induced apoptosis. *Oncogene* **34**, 485–495 (2015).
30. Tian, Z. et al. The deubiquitinating enzyme USP19 facilitates hepatocellular carcinoma progression through stabilizing YAP. *Cancer Lett.* **577**, 216439 (2023).
31. Scurr, L. L. et al. Ankyrin repeat domain 1, ANKRD1, a novel determinant of cisplatin sensitivity expressed in ovarian cancer. *Clin. Cancer Res.* **14**, 6924–6932 (2008).
32. Truvé, K. et al. Identification of candidate genetic variants and altered protein expression in neural stem and mature neural cells support altered microtubule function to be an essential component in bipolar disorder. *Transl. Psychiatry* **10**, 390 (2020).
33. Obara, Y. et al. ERK5 induces ankrd1 for catecholamine biosynthesis and homeostasis in adrenal medullary cells. *Cell Signal.* **28**, 177–189 (2016).
34. Mayor, R. & Theveneau, E. The neural crest. *Development* **140**, 2247–2251 (2013).
35. Baggiolini, A. et al. Premigratory and migratory neural crest cells are multipotent in vivo. *Cell Stem Cell* **16**, 314–322 (2015).
36. Wang, Z. et al. Identification of human cranio-maxillofacial skeletal stem cells for mandibular development. *Sci. Adv.* **11**, eado7852 (2025).
37. Egusa, H., Schweizer, F. E., Wang, C. C., Matsuka, Y. & Nishimura, I. Neuronal differentiation of bone marrow-derived stromal stem cells involves suppression of discordant phenotypes through gene silencing. *J. Biol. Chem.* **280**, 23691–23697 (2005).
38. Phi, J. H. et al. Expression of Sox2 in mature and immature teratomas of central nervous system. *Mod. Pathol.* **20**, 742–748 (2007).
39. Carniglia, L. et al. Melanocortin-receptor 4 activation modulates proliferation and differentiation of rat postnatal hippocampal neural precursor cells. *Neuropharmacology* **257**, 110058 (2024).
40. Sagar, S. M., Sharp, F. R. & Curran, T. Expression of c-fos protein in brain: metabolic mapping at the cellular level. *Science* **240**, 1328–1331 (1988).
41. Zheng, W. et al. NEATmap: a high-efficiency deep learning approach for whole mouse brain neuronal activity trace mapping. *Natl. Sci. Rev.* **11**, nwae109 (2024).
42. Gastfriend, B. D. et al. Notch3 directs differentiation of brain mural cells from human pluripotent stem cell-derived neural crest. *Sci. Adv.* **10**, eadi1737 (2024).
43. Aghaloo, T. L. et al. Osteogenic potential of mandibular vs. long-bone marrow stromal cells. *J. Dent. Res.* **89**, 1293–1298 (2010).
44. Sodek, J. & McKee, M. D. Molecular and cellular biology of alveolar bone. *Periodontol 2000* **24**, 99–126 (2000).
45. Wang, F. et al. Comparison of intraoral bone regeneration with iliac and alveolar BMSCs. *J. Dent. Res.* **97**, 1229–1235 (2018).
46. Mavropoulos, A., Rizzoli, R. & Ammann, P. Different responsiveness of alveolar and tibial bone to bone loss stimuli. *J. Bone Miner. Res.* **22**, 403–410 (2007).
47. Akintoye, S. O. et al. Skeletal site-specific characterization of orofacial and iliac crest human bone marrow stromal cells in same individuals. *Bone* **38**, 758–768 (2006).
48. Achilleos, A. & Trainor, P. A. Neural crest stem cells: discovery, properties and potential for therapy. *Cell Res.* **22**, 288–304 (2012).
49. Espinosa-Medina, I. et al. Neurodevelopment. Parasympathetic ganglia derive from Schwann cell precursors. *Science* **345**, 87–90 (2014).
50. Fox, D. et al. Crystal structure of the BARD1 ankyrin repeat domain and its functional consequences. *J. Biol. Chem.* **283**, 21179–21186 (2008).
51. Wolf, D. et al. Ankyrin repeat-containing N-Ank proteins shape cellular membranes. *Nat. Cell Biol.* **21**, 1191–1205 (2019).
52. Shi, D. J., Ye, S., Cao, X., Zhang, R. & Wang, K. Crystal structure of the N-terminal ankyrin repeat domain of TRPV3 reveals unique conformation of finger 3 loop critical for channel function. *Protein Cell* **4**, 942–950 (2013).
53. He, D., Zhang, M., Li, Y., Liu, F. & Ban, B. Insights into the ANKRD11 variants and short-stature phenotype through literature review and ClinVar database search. *Orphanet J. Rare Dis.* **19**, 292 (2024).
54. Islam, Z., Nagampalli, R. S. K., Fatima, M. T. & Ashraf, G. M. New paradigm in ankyrin repeats: beyond protein-protein interaction module. *Int. J. Biol. Macromol.* **109**, 1164–1173 (2018).
55. Mosavi, L. K., Minor, D. L. Jr. & Peng, Z. Y. Consensus-derived structural determinants of the ankyrin repeat motif. *Proc. Natl. Acad. Sci. USA* **99**, 16029–16034 (2002).
56. Gallagher, D. et al. Ankrd11 is a chromatin regulator involved in autism that is essential for neural development. *Dev. Cell* **32**, 31–42 (2015).
57. Roth, D. M. et al. The chromatin regulator Ankrd11 controls palate and cranial bone development. *Front. Cell Dev. Biol.* **9**, 645386 (2021).
58. Kibalnyk, Y. et al. The chromatin regulator Ankrd11 controls cardiac neural crest cell-mediated outflow tract remodeling and heart function. *Nat. Commun.* **15**, 4632 (2024).
59. Liu, H. et al. ANKRD11 binding to cohesin suggests a connection between KBG syndrome and Cornelia de Lange syndrome. *Proc. Natl. Acad. Sci. USA* **122**, e2417346122 (2025).
60. Lim, S. P. et al. Specific-site methylation of tumour suppressor ANKRD11 in breast cancer. *Eur. J. Cancer* **48**, 3300–3309 (2012).
61. Noll, J. E. et al. Mutant p53 drives multinucleation and invasion through a process that is suppressed by ANKRD11. *Oncogene* **31**, 2836–2848 (2012).
62. Vasmatzis, G. et al. Genome-wide analysis reveals recurrent structural abnormalities of TP63 and other p53-related genes in peripheral T-cell lymphomas. *Blood* **120**, 2280–2289 (2012).
63. He, Y. et al. 3D genome architecture in stem cell lineage commitment: from structural organization to precision regulation. *Adv. Genet.* **6**, e00035 (2025).
64. Zhang, H. et al. Nuclear FGF2 orchestrates phase separation-mediated rDNA chromatin architecture to control BMSCs cell fate. *Bone Res.* **13**, 80 (2025).
65. Kojic, S. et al. A novel role for cardiac ankyrin repeat protein Ankrd1/CARP as a co-activator of the p53 tumor suppressor protein. *Arch. Biochem. Biophys.* **502**, 60–67 (2010).
66. Henry, J. D., Grainger, S. A. & von Hippel, W. Determinants of social cognitive aging: predicting resilience and risk. *Annu. Rev. Psychol.* **74**, 167–192 (2023).
67. Kensinger, E. A. & Gutchess, A. H. Cognitive aging in a social and affective context: advances over the past 50 years. *J. Gerontol. B Psychol. Sci. Soc. Sci.* **72**, 61–70 (2017).
68. Bettio, L. E. B., Rajendran, L. & Gil-Mohapel, J. The effects of aging in the hippocampus and cognitive decline. *Neurosci. Biobehav. Rev.* **79**, 66–86 (2017).
69. Wang, C. L. et al. The mitochondrial unfolded protein response regulates hippocampal neural stem cell aging. *Cell Metab.* **35**, 996–1008.e1007 (2023).
70. Shetty, M. S., Sharma, M. & Sajikumar, S. Chelation of hippocampal zinc enhances long-term potentiation and synaptic tagging/capture in CA1 pyramidal neurons of aged rats: implications to aging and memory. *Aging Cell* **16**, 136–148 (2017).
71. Lovestone, S. & Imam, F. The GNPC provides a proteomic resource for biomarker discovery and mechanistic insight in neurodegenerative disease. *Nat. Aging* **5**, 1181–1185 (2025).
72. Chen, J. et al. Progressive reduction of nuclear receptor Nr4a1 mediates age-dependent cognitive decline. *Alzheimers Dement.* **20**, 3504–3524 (2024).
73. Cui, C. et al. Role of PTH1R signaling in Prx1(+) mesenchymal progenitors during eruption. *J. Dent. Res.* **99**, 1296–1305 (2020).
74. Wang, Z. et al. Deciphering the biological aging impact on alveolar bone loss: insights from α-Klotho and renal function dynamics. *J. Gerontol. A Biol. Sci. Med. Sci.* **79**, https://doi.org/10.1093/gerona/glae172 (2024).
75. Matsubara, T. et al. Alveolar bone marrow as a cell source for regenerative medicine: differences between alveolar and iliac bone marrow stromal cells. *J. Bone Miner. Res.* **20**, 399–409 (2005).

Open Access This article is licensed under a Creative Commons Attribution-NonCommercial-NoDerivatives 4.0 International License, which permits any non-commercial use, sharing, distribution and reproduction in any medium or format, as long as you give appropriate credit to the original author(s) and the source, provide a link to the Creative Commons licence, and indicate if you modified the licensed material. You do not have permission under this licence to share adapted material derived from this article or parts of it. The images or other third party material in this article are included in the article's Creative Commons licence, unless indicated otherwise in a credit line to the material. If material is not included in the article's Creative Commons licence and your intended use is not permitted by statutory regulation or exceeds the permitted use, you will need to obtain permission directly from the copyright holder. To view a copy of this licence, visit http://creativecommons.org/licenses/by-nc-nd/4.0/.

© The Author(s) 2026